Local diurnal wind-driven variability and upwelling in a small coastal embayment

Ryan K. Walter[1] (iD), Emma C. Reid[2] (iD), Kristen A. Davis[2], Kevin J. Armenta[1], Kevin Merhoff[3], and Nicholas J. Nidzieko[4]

[1]Physics Department, California Polytechnic State University, San Luis Obispo, California, USA, [2]Civil and Environmental Engineering, University of California, Irvine, California, USA, [3]Mechanical Engineering, California Polytechnic State University, San Luis Obispo, California, USA, [4]Department of Geography, University of California, Santa Barbara, California, USA

Abstract The oceanic response to high-frequency local diurnal wind forcing is examined in a small coastal embayment located along an understudied stretch of the central California coast. We show that local diurnal wind forcing is the dominant control on nearshore temperature variability and circulation patterns. A complex empirical orthogonal function (CEOF) analysis of velocities in San Luis Obispo Bay reveals that the first-mode CEOF amplitude time series, which accounts for 47.9% of the variance, is significantly coherent with the local wind signal at the diurnal frequency and aligns with periods of weak and strong wind forcing. The diurnal evolution of the hydrographic structure and circulation in the bay is examined using both individual events and composite-day averages. During the late afternoon, the local wind strengthens and results in a sheared flow with near-surface warm waters directed out of the bay and a compensating flow of colder waters into the bay over the bottom portion of the water column. This cold water intrusion into the bay causes isotherms to shoal toward the surface and delivers subthermocline waters to shallow reaches of the bay, representing a mechanism for small-scale upwelling. When the local winds relax, the warm water mass advects back into the bay in the form of a buoyant plume front. Local diurnal winds are expected to play an important role in nearshore dynamics and local upwelling in other small coastal embayments with important implications for various biological and ecological processes.

1. Introduction

Nearshore coastal environments of eastern boundary current upwelling systems, such as the California Current Large Marine Ecosystem (CCLME), are among the world's most productive ecosystems. The intense productivity of these systems is shaped by physical processes on a wide range of spatiotemporal scales, ranging from regional-scale (100 s of km) to local-scale (10 s of km and smaller) processes. On a regional scale, prevailing atmospheric conditions in the CCLME drive equatorward winds, resulting in seasonal coastal upwelling [cf. *Hickey*, 1979]. This process brings deep, cold, nutrient-rich waters close to the surface, nourishing near-surface phytoplankton and fueling nearshore productivity [*Pennington and Chavez*, 2000]. During the major upwelling season in CA (approximately April–September [*García-Reyes and Largier*, 2012]), strong upwelling favorable winds (typically lasting weeks) drive intrusions of offshore waters into the nearshore region. This process is interrupted during regional wind relaxation events lasting several days [e.g., *Send et al.*, 1987] that allow warm offshore waters to move back toward the coast and in some cases poleward [cf. *Washburn et al.*, 2011]. These upwelling/relaxation cycles have been linked to the delivery of invertebrate larvae to nearshore habitats [*Roughgarden et al.*, 1991; *Wing et al.*, 1995] and are often times thought of as the dominant feature driving variability and affecting a host of physical and biological processes along large portions of the CCLME [*Hickey*, 1979; *Breaker and Broenkow*, 1994; *Pennington and Chavez*, 2000; *Woodson et al.*, 2009; *García-Reyes and Largier*, 2012; *Cheriton et al.*, 2014; *Walter et al.*, 2014b; *Walter and Phelan*, 2016].

Local features, however, may play an equally important role in driving ecosystem dynamics in the coastal ocean, particularly with regard to local wind-driven variability, coastline orientation, and topography. For example, in northern Monterey Bay, a large open coastal embayment located along the central California coast, a persistent coastal upwelling front forms between cold, recently upwelled waters outside the bay

and warm, trapped waters inside of the bay that are shadowed (i.e., "upwelling shadow" [*Graham and Largier*, 1997; *Woodson et al.*, 2009; *Bonicelli et al.*, 2014a]) from regional wind forcing by topographic features (i.e., Santa Cruz Mountains) [*Woodson et al.*, 2009]. The upwelling front propagates back and forth along the coast daily due to modulation by strong diurnal wind forcing [*Woodson et al.*, 2009; *Walter et al.*, 2016]. In the northern portions of the bay, the local sea breeze is oriented parallel to the coastline, resulting in an offshore Ekman transport of surface waters and local diurnal upwelling [*Woodson et al.*, 2007]. In a smaller open embayment along the coast of Chile (Cartagena Bay), *Bonicelli et al.* [2014a] found that northern and southern bay sites, separated by just 6 km, experienced markedly different thermal structure and current variability due to the presence and absence, respectively, of strong local diurnal wind forcing.

On local scales, diurnal winds can be driven by differential heating and cooling between the land and ocean, as well as topographic steering [*Gille et al.*, 2003, 2005]. These sea (and land) breezes are common in coastal zones worldwide and can have a significant effect on nearshore physical and biological variability. For example, several studies have found that diurnal wind forcing is a major mechanism driving significant temperature oscillations, some of which are on the order of seasonal fluctuations [*Kaplan et al.*, 2003; *Woodson et al.*, 2007; *Bonicelli et al.*, 2014a; *Aristizabal et al.*, 2016]. Local winds have also been shown to influence a host of physical processes including local diurnal upwelling [*Woodson et al.*, 2007], inertial current oscillations [*Orlić et al.*, 2011; *Lucas et al.*, 2014], internal wave development [*Lerczak et al.*, 2001], local heat budgets [*Suanda et al.*, 2011], modulation of buoyant plume fronts and the subsequent evolution of nonlinear internal waves [*Woodson et al.*, 2009; *Walter et al.*, 2016], and local circulation patterns [*Rosenfeld*, 1988; *Woodson et al.*, 2007; *Bonicelli et al.*, 2014a]. From a biological perspective, local diurnal winds have been shown to play a fundamental role in phytoplankton dynamics [*Lucas et al.*, 2014] and spatial patterns of barnacle settlement [*Bonicelli et al.*, 2014b], thereby affecting ecosystem productivity and the transport of larvae. Despite this growing list, a deeper understanding of the ubiquity and importance of these local-scale processes at regional and global scales is still lacking.

Our goal here is to document in detail the fine-scale (both spatial and temporal) oceanic response of a small (bay length scale L ~ 2 km in this study) coastal embayment that is characteristic of the coastline along the CCLME and other boundary current systems. In this contribution, we focus on the effect of local diurnal wind forcing on temperature variability, circulation patterns, and upwelling dynamics in a small coastal embayment located along an understudied stretch of the central California coast. Extension of the results and their implications, along with recommendations for future work and modeling studies, are discussed.

2. Experimental Setup and Methods

2.1. Field Site and Data

San Luis Obispo (SLO) Bay is a small semienclosed coastal embayment located along the eastern Pacific Ocean and the central California coast (Figure 1a). The northern portion of SLO Bay (L ~ 2 km wide), and the focus of this study, is sheltered behind several prominent coastal peaks and topographic features and so is sheltered from regional northwesterly winds (Figure 1c). SLO Bay and the surrounding region feature a vast ecological diversity including giant kelp forests, several popular tourist destinations, and beaches (e.g., Avila Beach, Pismo Beach), a major fishing port (Port San Luis) for local fisheries (e.g., rockfish, Dungeness crab), and the California Polytechnic State University (Cal Poly) Pier (Figure 1c). The surrounding region is also home to several State Marine Reserves and Conservation Areas and is part of the proposed Chumash Heritage National Marine Sanctuary. To date, there has not been a comprehensive study examining nearshore physical processes and the effect of local wind forcing on circulation patterns in SLO Bay.

In order to assess the influence of local wind forcing on temperature and current variability and local upwelling dynamics, a cross-shelf array of three oceanographic moorings was deployed at the northern end of SLO Bay from 23 June to 12 August 2015. The main mooring was deployed near the 16.5 m isobath in the center of the study site region (Middle Bay, Figure 1c) and included the following instrumentation: thermistors (RBRsolo T, accuracy of 0.002°C) sampling at 2 Hz placed every meter in the vertical from 1 m above the bed (mab) to 13 mab; a Sea-Bird 37 conductivity-temperature-depth (CTD) sensor sampling at 3 min intervals located at 2 mab; and a Teledyne RDI Sentinel V (1000 kHz, five beams) acoustic Doppler current profiler (ADCP) colocated next to the mooring line. The ADCP sampled continuously at 2 Hz with 0.4 m vertical bin spacing and was leveled by divers to within 1° of the horizontal to minimize instrument tilt errors.
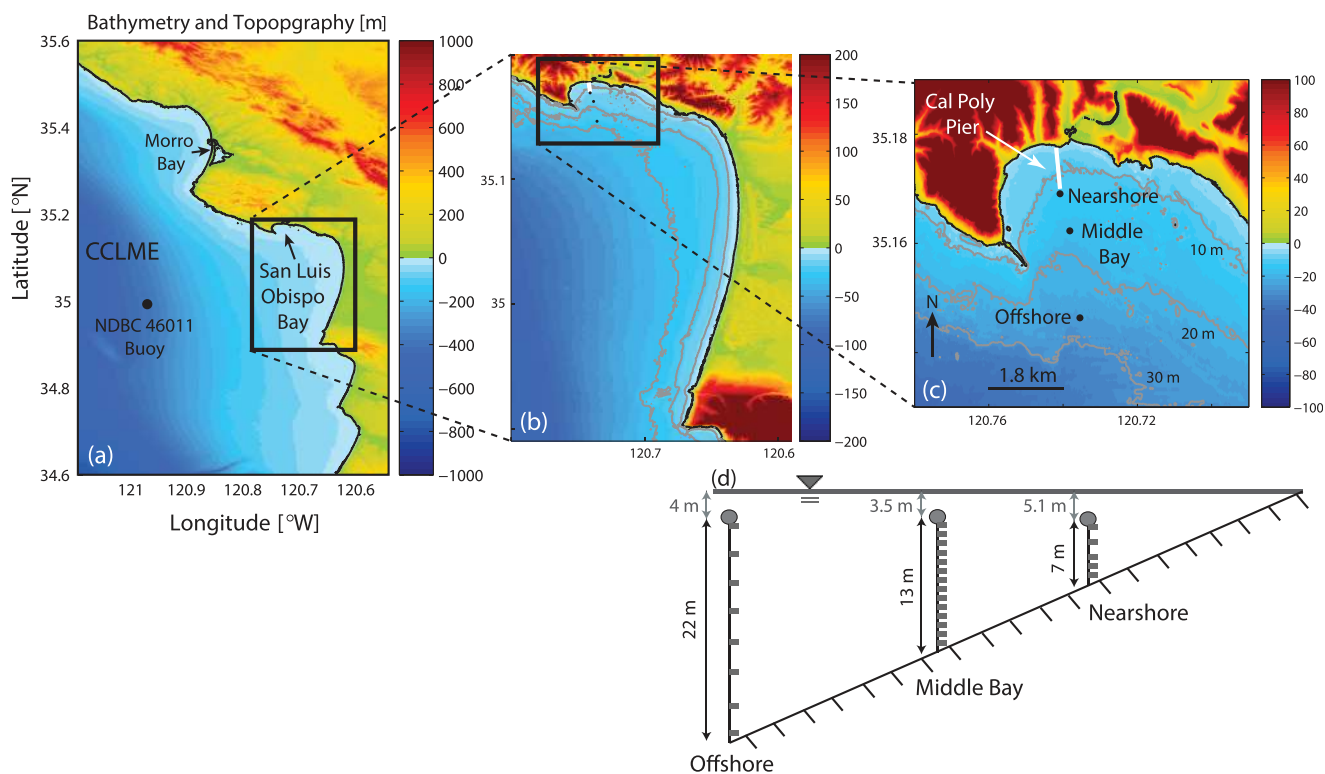
Figure 1. (a) Bathymetry and topography of the greater SLO Bay region highlighting the location of the offshore buoy used for regional wind data (black dot, NDBC 46011). (b, c) Zoomed in maps highlighting the nearshore study site in SLO Bay and the location of instrumented moorings (black dots) and the Cal Poly Pier (solid white line). The gray lines denote the 10, 20, and 30 m isobaths. (d) Schematic of the cross-shelf array of moorings and instrumentation, where the gray rectangles denote approximate thermistor locations, the gray circle indicates the subsurface buoy location, and the black and gray lengths designate the vertical distance from the seafloor to the near-surface thermistor, and the approximate vertical distance from the near-surface thermistor to the average sea surface height over the experiment, respectively.

An additional mooring was deployed offshore of the Middle Bay mooring near the 26 m isobath to capture the offshore extent of the northern bay region (offshore, Figure 1c). This mooring contained thermistors (RBRsolo T, 2 Hz sampling) with 3 m vertical spacing spaced from 1 to 22 mab (1, 4, 7, 10, 13, 16, 19, and 22 mab), as well as Sea-Bird 37 CTD sensors at 2 and 19 mab. A shallow nearshore mooring was deployed close to the 12 m isobath at the end of the Cal Poly Pier (nearshore, Figure 1c) with thermistors (RBRsolo T, 2 Hz sampling) at 1, 2, 3, 5, and 7 mab. The configuration of the moorings was designed to capture upwelling processes and the cross-shelf evolution of temperature (Figure 1d).

In order to examine regional wind forcing, offshore winds were obtained from the National Data Buoy Center (NDBC) buoy 46011 (Figure 1a; http://www.ndbc.noaa.gov/station_page.php?station=46011) and rotated to upwelling favorable winds (i.e., equatorward and parallel to the regional coastline, 150° from true north). Meteorological data, including local wind data inside the northern area of SLO Bay, were obtained from measurements (2 min intervals) collected at the end of the Cal Poly Pier (Figure 1c).

To assess regional-scale variability, a Level 4 (blended) sea surface temperature (SST) product was acquired. This product was produced on a global 0.011° grid by the Group for High Resolution Sea Surface Temperature (GHRSST) at the Jet Propulsion Laboratory. This Multiscale Ultrahigh Resolution (MUR) Level 4 analysis (version 4) is based upon nighttime GHRSST Level 2 skin and subskin SST observations from a host of instruments including the NASA Advanced Microwave Scanning Radiometer-EOS, the Moderate Resolution Imaging Spectroradiometer on the NASA Aqua and Terra platforms, the US Navy microwave WindSat radiometer, and in situ SST observations from the NOAA iQuam project (http://podaac.jpl.nasa.gov; accessed 6 October 2015). Ocean surface current data were obtained via a regional network of high-frequency (HF) radar data. Data (2 km gridded) were downloaded from the Coastal Observing Research and Development Center at Scripps Institution of Oceanography (http://hfrnet.ucsd.edu/thredds/catalog.html; accessed 22 October 2015). All times referenced in the text and figures are in local time [Pacific Daylight Time (PDT)].

2.2. Data Analysis

Spectral and coherence calculations were carried out using standard techniques [e.g., *Walter et al.*, 2011]. The window length was selected by taking into account the length of the original record, frequency resolution, and the degrees of freedom (DOF) for calculating confidence intervals. In order to minimize leakage in the spectral domain, Hamming windows with 50% overlap were applied. A chi-square variable analysis was performed using the equivalent DOF to calculate confidence intervals on the spectra [*Emery and Thomson*, 2001]. Statistical significance in the coherence analysis was also calculated using the equivalent DOF [*Emery and Thomson*, 2001].

The time-varying frequency content (power) of various time series was examined using continuous wavelet transforms following *Torrence and Compo* [1998]. A Morlet mother wavelet function was used with a nondimensional frequency parameter (ω_o as in *Torrence and Compo* [1998]) set to six in order to satisfy necessary conditions for the wavelet function. The wavelet power spectrum is defined using the magnitude of the wavelet transform squared, $W = |W_n(s)|^2$, where n is a localized time index and the wavelet scale (s) is almost identical to the Fourier period. In order to isolate the time-varying wavelet power over a particular band of scales (periods), such as the diurnal period, the scale-averaged wavelet power is calculated between scales (s_1 to s_2) using the following formula:

$$\langle W(t) \rangle = \frac{\delta j \delta t}{C_\delta} \sum_{j=j_1}^{j_2} \frac{\left| W_n\left(s_j\right) \right|^2}{s_j}, \tag{1}$$

where δj is the scale resolution, δt is the sampling time interval, and $C_\delta = 0.776$ is a reconstruction constant. To determine confidence levels, wavelet power is compared to a background model spectrum of red-noise (i.e., univariate lag-1 autoregressive; see *Torrence and Compo* [1998] for additional details).

A complex empirical orthogonal function (CEOF) analysis was used to decompose the ADCP velocity data into its dominant statistical modes (i.e., its principal components). The CEOF analysis was applied to the complex time series $\psi(z, t) = u(z, t) + iv(z, t)$, where u and v represent the eastward and northward components of velocity, respectively, and $i = \sqrt{-1}$. By solving an eigenvalue problem for the complex covariance matrix (formed using the time varying portion of $\psi(z, t)$), the CEOF analysis provides a description of the spatial variability of the velocity field through modal shapes (i.e., eigenfunctions), as well as the temporal variability of each independent vertical mode through a complex amplitude time series [*Kaihatu et al.*, 1998; *Edwards and Seim*, 2008]. Moreover, the eigenvalue associated with each respective modal shape can be used to quantify the contribution of that modal shape to the total variance of the original signal. Using a complex analysis has the benefit of a more physical interpretation to a particular phenomenon since the modal shape not only dilates and contracts in time based on the magnitude of the complex amplitude time series, but it also rotates in time using the phase (i.e., angle) of the complex amplitude time series (real component eastward, imaginary component northward) [*Edwards and Seim*, 2008].

3. Results

3.1. General Observations

Throughout the nearly 2 month long study period, offshore winds exhibited typical regional upwelling/relaxation cycles (Figure 2a) for the central California coast [*Woodson et al.*, 2009; *Walter et al.*, 2014b; *Walter and Phelan*, 2016], with persistent upwelling winds blowing from 330° for several weeks alternating with several days of reduced wind speeds. The local wind forcing consistently displayed diurnal fluctuations with eastward wind components reaching more than 10 m/s during the afternoon (Figures 2a and 2b). The westward component was much weaker and often nonexistent. The local diurnal wind signal also displayed periods of stronger/weaker variability throughout the record.

The vertical temperature structure recorded at the cross-shelf array of moorings shows several prominent features (Figures 2c–2e). The first is the presence of cold (and saltier, S 33.7) waters extending throughout the water column at the beginning of the record and the appearance of a warm (and fresher, S 33.4) water mass toward the end of July. SST images indicate that these cold and warm water masses are the result of regional water masses advected into SLO Bay from the north and south/offshore, respectively (Figure 2h). The cold water mass is likely the result of extended regional upwelling lasting several weeks prior
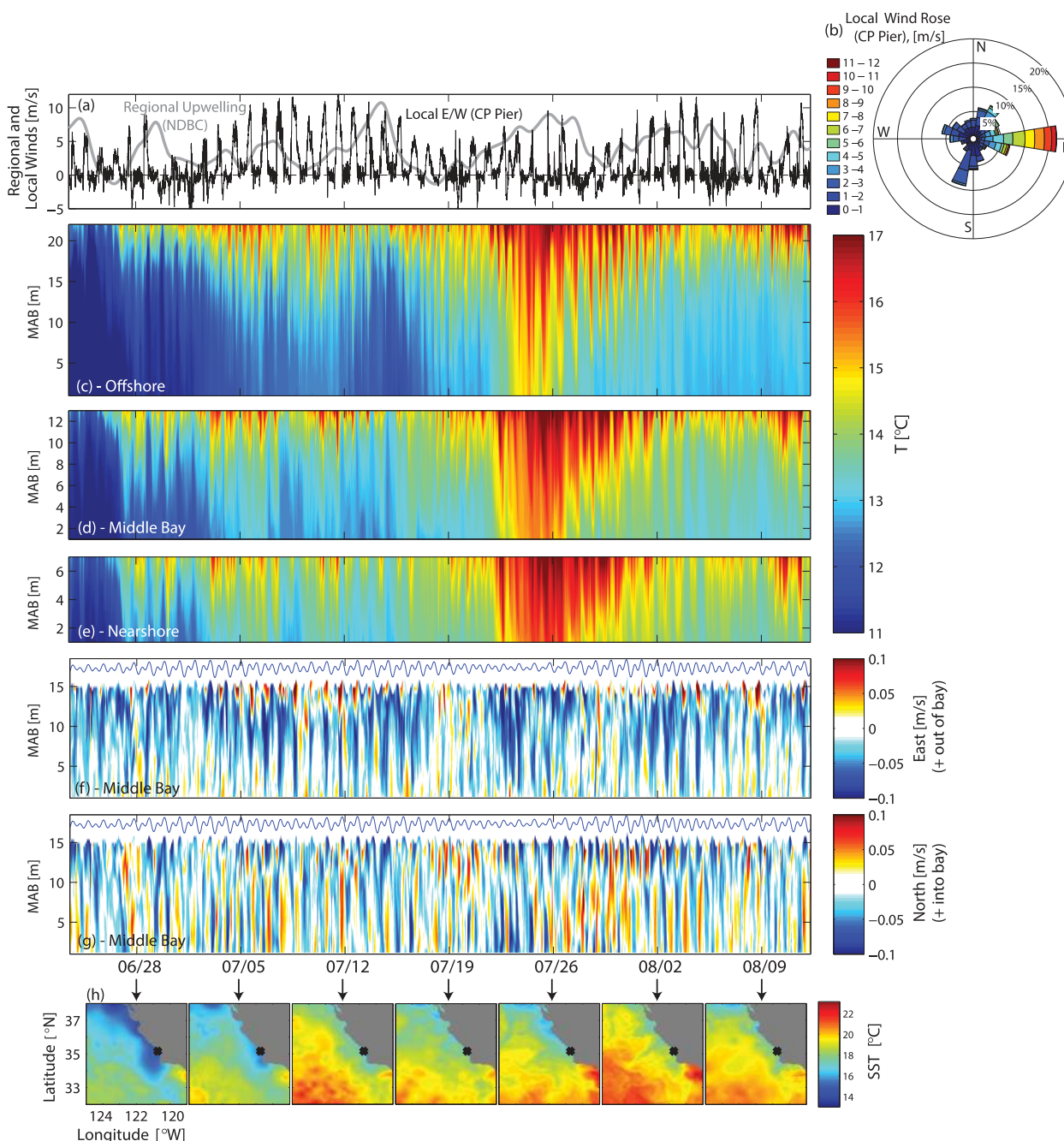
Figure 2. (a) Regional upwelling favorable winds from NDBC buoy 46011 (33 h low-pass filtered, gray line) and local east/west (positive = eastward) winds from the Cal Poly Pier (black line). (b) Local wind rose (oceanographic orientation-directionality indicates wind vector direction) using data from the Cal Poly Pier. Time series of the vertical temperature structure (10 min averages) at the (c) Offshore, (d) Middle Bay, and (e) Nearshore moorings. (f) East/west (positive = eastward/out of the bay study site) and (g) north/south (positive = northward/into the bay study site) time series of the vertical velocity structure (60 min averages) from the Middle Bay mooring. The solid blue line in Figures 2f and 2g denotes the sea surface height. (h) Weekly MUR SST images corresponding to the dates shown on the bottom of Figure 2g. The black "x" in Figure 2h denotes the study site location.

to the start of the observations (not shown), while the warm water mass appears to originate from the combination of a poleward warm water flow from south of Point Conception [*Washburn et al.*, 2011] and the intrusion of offshore waters that originate from submesoscale features [*Nidzieko and Largier*, 2013]. The second prominent feature, and the focus of this study, is higher-frequency variability that results in large daily temperature fluctuations (up to 5°C) on the same order of those driven by regional water mass advection, and the associated appearance of strong frontal features that result in the episodic stratification of the water column. This high-frequency temperature variability is coherent across the three mooring sites, and

in some cases, results in perturbations that extend throughout the entire water column at the nearshore site, especially during strong local wind forcing. These features coincide with near-surface velocities directed out of the bay study site and the development of surface-intensified velocity shear (Figures 2f and 2g), particularly during periods of enhanced local wind forcing.

A closer examination of a representative 2 day period (6 and 7 July 2016) from the Middle Bay mooring reveals the diurnal evolution of the aforementioned high-frequency features (Figure 3). During the early morning when the local winds are absent, a near-surface warm water mass in the form of a buoyant plume front advects in the northwest direction (i.e., directly into the northern portion of the bay, black arrows in Figure 3), resulting in strong near-surface stratification. The resulting stratification provides an internal wave guide and supports high-frequency (i.e., 5–30 min period) internal wave activity [*Walter et al.*, 2016]. During the late morning, a local eastward wind develops, peaking in the early afternoon, and subsiding in the late evening. This period of strong local wind forcing is characterized by the development of near-surface flow reversals, as the currents at the top of the water column start to move toward the southeast (i.e., out of the northern portion of the bay, red arrows in Figure 3), driving the surface warm water mass out of the bay. While the surface currents are directed out of the northern bay, a compensating flow directly into the bay exists over the bottom portion of the water column. The result is a strong baroclinic flow with increased shear in the near-surface region. This northwestward flow along the bottom drives colder waters into the northern end of the bay (gray arrows in Figure 3). These cold waters infiltrate throughout the water column and shoal toward the surface, replacing the warm surface layer. Following this local wind-driven modulation and upwelling, the local winds relax, allowing the warm water mass to advect back into the northern bay.
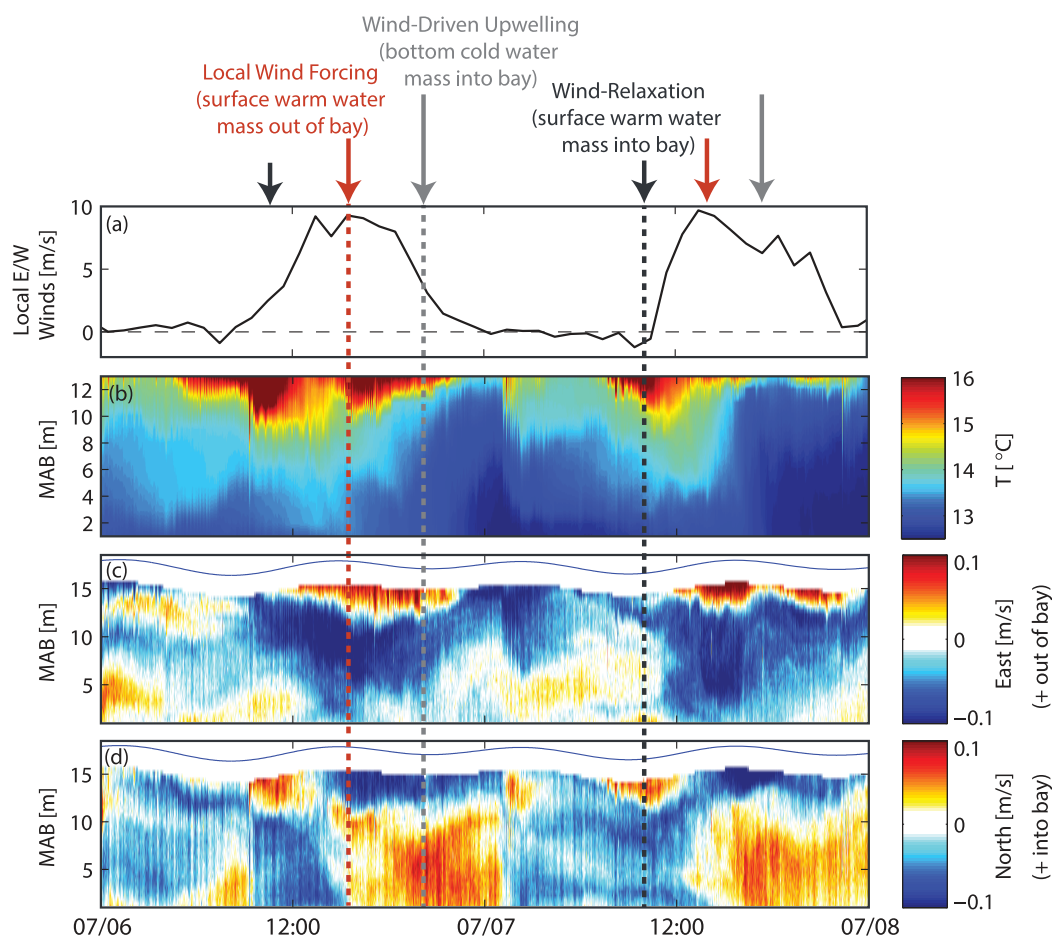

Figure 3. Zoomed in time series example from 6 and 7 July 2016 of the (a) local east/west winds (east = positive), (b) vertical temperature structure (1 min averages), and the (c) east/west (positive = east/out of the bay study site), and (d) north/south (positive = north/into the bay study site) velocity (1 min averages) throughout the water column at the Middle Bay mooring. The solid blue line in Figures 3c and 3d denotes the sea surface height.
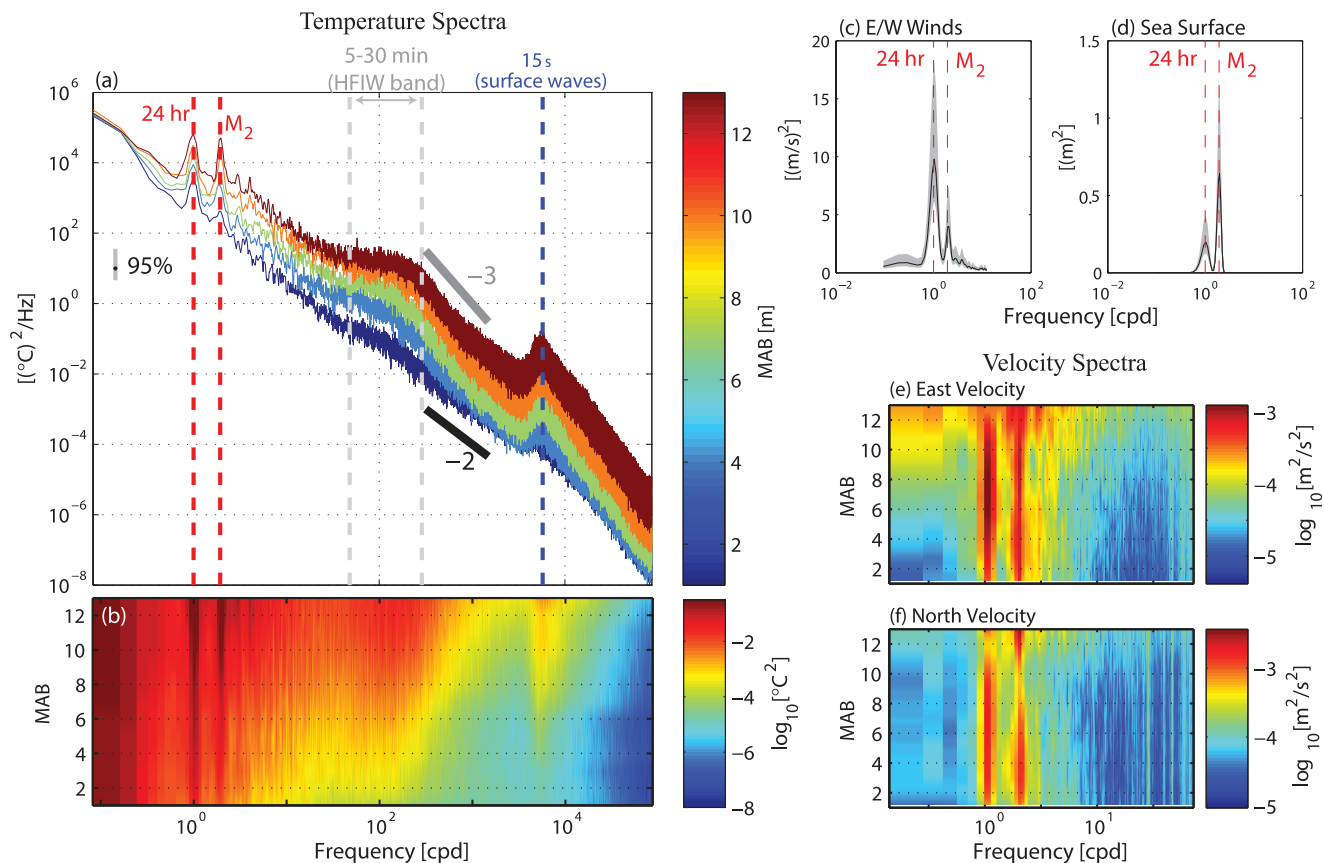
Figure 4. (a) Power spectral density of temperature at discrete heights (denoted in color bar) throughout the water column at the Middle Bay mooring. The dashed red lines denote the diurnal and semidiurnal (M_2 tidal component) frequencies, the dashed gray lines the high-frequency internal wave band, and the dashed blue line the surface wave frequency. Also shown is a −3 (solid gray) and −2 (solid black) power law fit. (b) Variance preserving power spectra of temperature at all vertical locations. Variance preserving power spectra of the (c) local east/west winds and the (d) local sea surface height. The dashed red lines in Figures 4c and 4d denote the diurnal and semidiurnal (M_2 tidal component) frequencies and the gray shading signifies 90% confidence intervals. Variance preserving power spectra of the (e) east and (f) north velocity components throughout the water column.

Consideration of the temperature spectra across various depths reveals a major, surface-intensified peak at the diurnal frequency, with a weaker signal in the semidiurnal band (Figures 4a and 4b). The local east/west winds also show a dominant diurnal peak (Figure 4c). The temperature spectra of near-surface thermistors display enhanced variance within the high-frequency internal wave (HFIW) band (5–30 min period). At frequencies higher than the HFIW band, the spectral falloff rate follows a −3 power law fit in the upper water column and transitions to the more canonical −2 power law fit at the bottom of the water column, implying a strong scattering of near-surface HFIWs toward smaller scales in the near-surface region [*Nam and Send*, 2012]. The velocity spectra as a function of depth also reveal a prominent peak in the diurnal band, particularly in the east velocity component which is aligned with the direction of the local wind forcing (Figures 4e and 4f).

3.2. Velocity Variance and Winds
A tidal harmonic analysis was performed on the velocity observations over the entire study period (not shown) using the T_Tide package [*Pawlowicz et al.*, 2002]. The north and east velocity components (60 min averages) were separated into their barotropic and baroclinic components using depth-averaged values. The K_1 (diurnal) and M_2 (semidiurnal) tidal components dominated the barotropic signal, although the tidal ellipses only had semimajor axes on the order of 1 cm/s for each component, indicating weak barotropic tidal forcing. For the baroclinic component, tidal ellipses were calculated as a function of depth for the K_1 and M_2 components. The M_2 component displayed semimajor and semiminor axes that were approximately constant with depth and O(1 cm/s), again indicating weak semidiurnal tidal forcing. The K_1 tidal ellipse exhibited near-surface semimajor (4.6 cm/s) and semiminor (2.2 cm/s) axes that were enhanced relative to the bottom of the water column [both near-bottom axes O(1 cm/s)]. The surface tidal ellipses were also

approximately 180° out of phase from the bottom ellipses and oriented with the prevailing bay coastline orientation (i.e., 30–50° CCW from true north).

The large baroclinic K_1 amplitudes computed with the harmonic analysis are likely due to signal contamination of the diurnal band by strong local winds [cf. *Rosenfeld et al.*, 2009; *Suanda et al.*, 2011]. This is evident as a decrease in amplitude with depth, consistent with frictional forcing from above, as well as the findings from the nearby Monterey Bay region [see *Rosenfeld et al.*, 2009, discussion; *Suanda et al.*, 2011]. Moreover, at this particular latitude (35.17°N), which is poleward of the critical latitude (30°N), the diurnal frequency (1 cpd) is smaller than the inertial frequency (f 1.15 cpd). Thus, freely propagating internal waves at the diurnal frequency are not permitted, given that the background current vorticity is likely small [cf. *Lerczak et al.*, 2001; *Aristizabal et al.*, 2016]. Moreover, a coherence analysis was performed using the local winds and the east baroclinic velocity component as a function of depth. At the diurnal frequency, the winds and velocity were significantly coherent with approximately zero phase lag at the surface (not shown). Further validation that the currents are predominantly driven by local winds is presented below using the CEOF analysis and comparison of strong versus weak local wind forcing periods.

The first modal shape of the CEOF analysis, which describes 47.9% of the total velocity variance, shows a sheared, baroclinic structure with a very near-surface layer that is roughly 180° out of phase with the rest of the water column (Figure 5a). The magnitude of the amplitude time series shows temporal variability that is generally aligned with periods of enhanced variance in the east/west winds time series time (described further below; Figure 5b). The first three modes describe 90% of the variance, but as will be discussed below, the first mode displays a diurnal variability that is coherent with the local wind forcing and thus will be the focus of what follows.

A wavelet analysis of the first-mode CEOF amplitude time series magnitude, which dilates and contracts the CEOF modal shape over time, was performed to examine the time-varying frequency content of the time series. Figure 6b shows that the first-mode CEOF amplitude magnitude is dominated by the diurnal frequency band. The temporal variability in the diurnal variance also aligns with the majority of the diurnal peaks in the local east/west wind field. A similar alignment of the diurnal peaks is not seen between the first-mode CEOF amplitude time series magnitude and the local sea surface height (Figure 6c), indicating that the first-mode CEOF is modulated by the local wind forcing and not by surface tidal forcing. Scale-averaged wavelet power was calculated between 22 and 26 h for the local winds, the first-mode CEOF amplitude time series magnitude, and the local sea surface height, in order to isolate the contribution to the diurnal frequency band. The scale-averaged power is normalized by the maximum value for each respective variable for comparison between variables (Figure 6d). Evident in the diurnal power is a strong
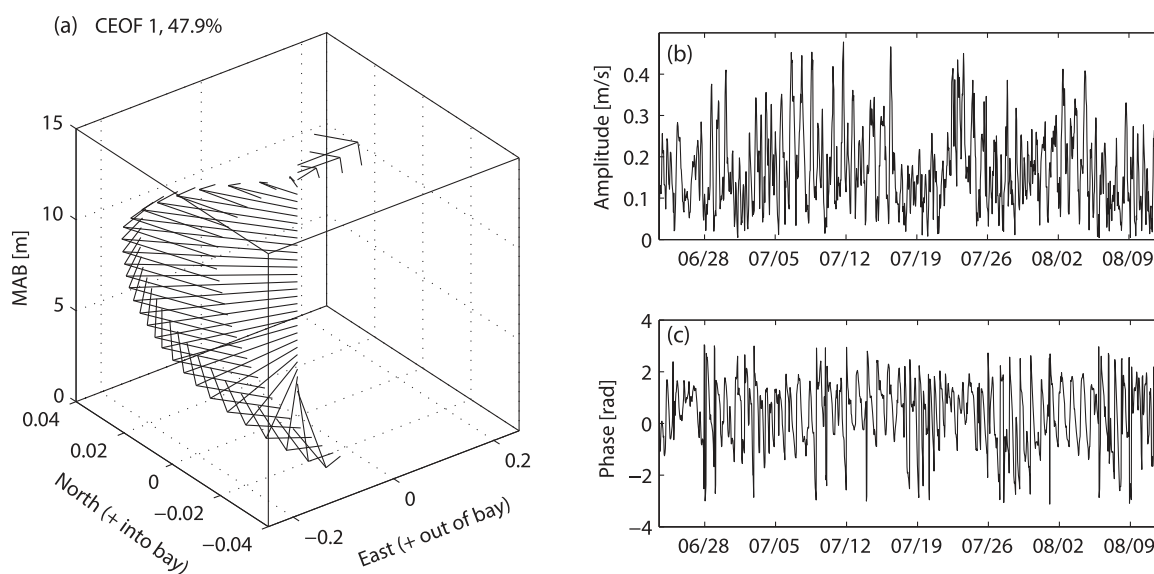

Figure 5. First-mode CEOF (explains 47.9% of the variance) from the Middle Bay mooring. (a) Modal shape (real component, eastward), (b) magnitude of the complex amplitude time series, and (c) phase (i.e., angle of the complex amplitude time series, where the angle is measured CCW from the positive real axis).
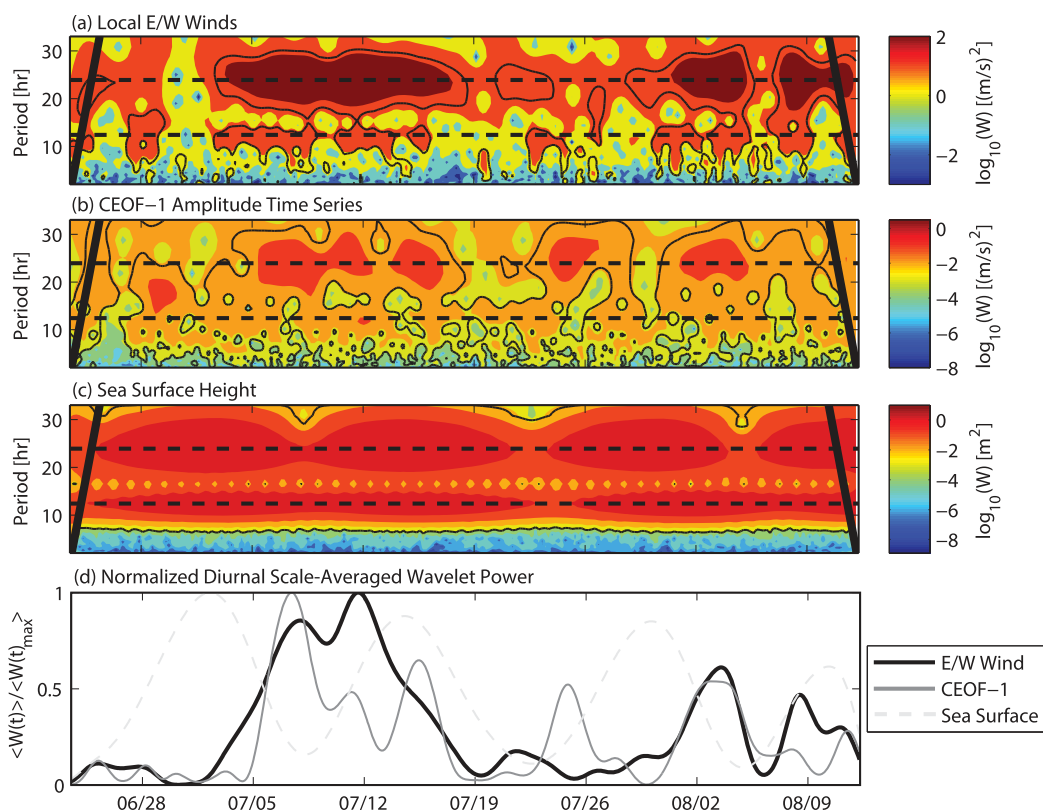
Figure 6. Wavelet power spectrum of the (a) local east/west winds, (b) amplitude time series from the first-mode CEOF, and (c) the local sea surface height. The black contour lines represent the 90% confidence level. The dashed black lines denote the diurnal and semidiurnal (M_2 tidal component) periods. Thick black lines on both ends of the spectrum indicate the "cone of influence" where edge effects become important. (d) Scale-averaged wavelet power between periods of 22 and 26 h isolating the diurnal band for each variable in Figures 6a–6c. The scale-averaged wavelet power is normalized by the maximum value for each respective variable for comparison between the variables.

correlation between the local winds and the first-mode CEOF amplitude time series magnitude, with a pronounced peak in the two variables in the middle of July. The local winds and amplitude time series magnitude are significantly coherent at the diurnal frequency (Figure 7a) with almost zero phase lag (Figure 7b). Moreover, the temporal variability in the diurnal band of the local sea surface height does not correspond to the diurnal variance in the first-mode CEOF (or the local wind, Figure 6d), nor are the two parameters coherent at the diurnal frequency (Figure 7a). The above evidence suggests that the first-mode CEOF signal, which describes nearly half the velocity variance, is largely determined by local wind forcing in the northern portion of the bay.

3.3. Canonical Day and the Diurnal Cycle

In order to assess the diurnal cycle of the local wind forcing, circulation, and temperature structure, canonical day (i.e., composite averages representing a typical day) plots were created by computing averages of variables centered on each hour of the day (local time, PDT) at the Middle Bay mooring. Figure 8 highlights the diurnal evolution of various parameters and further clarifies the trends discussed previously. During the morning hours (~00:00–08:00), the local wind forcing is absent (Figure 8a) and a warm surface layer appears at the study site as a buoyant plume front that increases local stratification (Figure 8d). The arrival of this warm front corresponds with near-surface velocities directed mainly into the bay (i.e., toward the west, Figures 8e and 8f). As the local eastward winds develop in the late morning and peak around 15:00, a strong jet oriented out of the bay study site (i.e., southeastward) develops near the surface. This offshore flow near the surface coincides with the arrival of a large intrusion of cold water over the bottom portion of the water column with velocities oriented into the bay study site (northwestward). This cold water intrusion into the bay study site causes isotherms to shoal toward the surface and represents a mechanism for local wind-driven diurnal upwelling distinct from the classic coastal upwelling described by Ekman-like dynamics. In
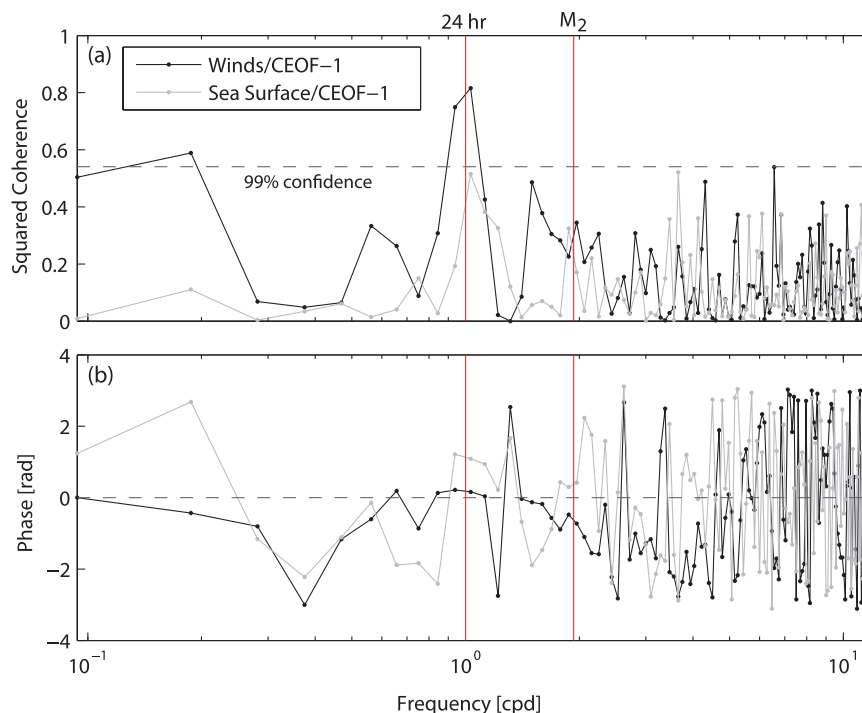
Figure 7. (a) Coherence squared and (b) phase lag between the local winds and the first-mode CEOF amplitude time series (black), as well as the local sea surface height and the first-mode CEOF amplitude time series (gray). The 99% confidence level is shown as a gray line in Figure 7a. The diurnal and semidiurnal (M_2 tidal component) frequencies are denoted by red lines.

this case, the shoaling of isotherms is related to the advection of cold subsurface waters, which originate outside of the shallow portions of the embayment, into the study site location (i.e., an undercurrent [see *Kämpf*, 2015a,2015b, and references therein]) due to diurnally varying currents forced by the local winds. Temperature and velocity variability over the canonical day (Figures 8g and 8h), quantified by calculating the standard deviation at each canonical day hour, is concentrated in the surface layer. This is likely due to a combination of changes in the frontal structure, HFIW activity, and variability in the local wind forcing (i.e., stronger and weaker local wind forcing periods), the latter of which is explored further below.

The first-mode CEOF amplitude time series magnitude, which dilates/contracts the modal shape in Figure 5a, follows the diurnal cycle and evolution of the local winds, peaking around 15:00 (Figure 8b). The phase (i.e., angle of the complex amplitude time series) of the first-mode CEOF, which rotates the modal shape in Figure 5a, follows the dominant velocity trends described above. For example, during peak wind forcing when the magnitude of the amplitude time series is at its maximum (i.e., large dilation of the modal shape in Figure 5a), the phase is close to zero and begins to go slightly negative in later hours [negative (positive) phase indicate CW (CCW) rotation of the modal shape]. Taken into consideration with the modal shape, this phasing is consistent with the southeast (northwest) flow that develops near the surface (bottom) of the water column. The diurnal evolution of the phase, and the corresponding rotation of the modal shape, is also consistent with the velocity signal directionality at other times. Composite day averages of the second-mode CEOF (30.8% of velocity variance explained, not shown) display a constant amplitude and phase over all composite day hours, indicating that this mode is not forced by diurnal winds. The local diurnal winds appear to be a first order control on the dominant circulation patterns, temperature variability, and upwelling inside the bay.

The diurnal evolution of ocean surface currents throughout the entire bay region, as opposed to just the northernmost portion of the bay where the in situ moorings were located, was assessed using canonical day averages of HF radar measurements over 3 h periods (Figure 9). We note that only qualitative inferences can be made with the HF radar measurements and that the gridded measurements (i.e., 2 km) may not sufficiently resolve all fine-scale features and local forcing effects, particularly at points close to the coastline. Nonetheless, during the early parts of the day when the local winds are weak, surface currents are generally
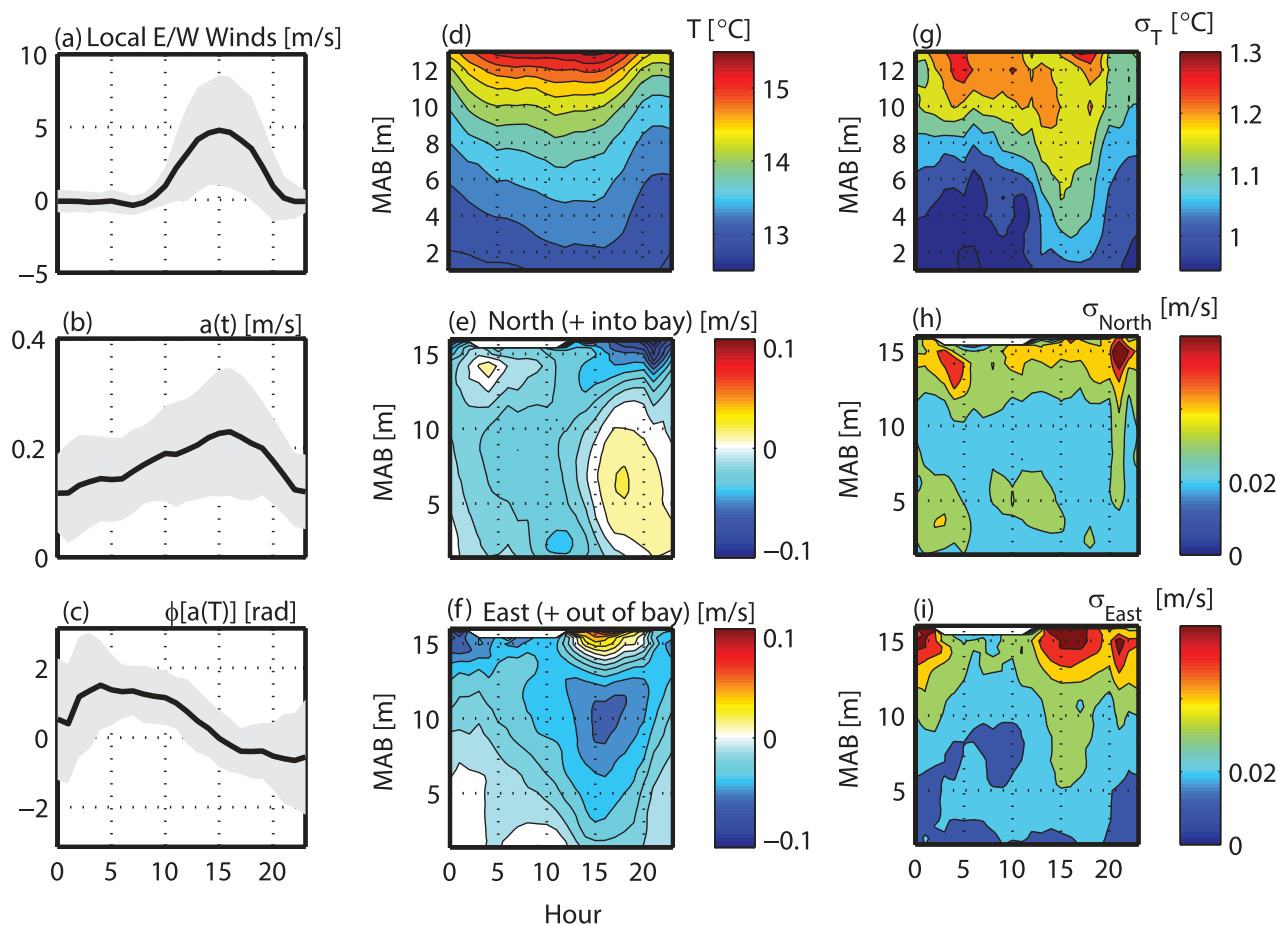
Figure 8. Composite day average plots over the entire study period of the (a) local east/west winds, (b) first-mode CEOF amplitude time series magnitude, and the (c) first-mode CEOF phase. The gray shading signifies one standard deviation from mean. Composite day contour plots from the Middle Bay mooring of (d) temperature, (e) north/south velocity (positive = north/into the bay study site), and (f) east/west velocity (positive = east/out of the bay study site). Figures 8g–8i denote the standard deviation of the respective quantity in Figures 8d–8f.

weak (especially from 03:00 to 09:00). During the late afternoon, the surface currents increase in strength and show a large-scale flow directed out of the greater embayment area and directed to the south.

3.4. Weak Versus Strong Local Wind Forcing

The effect of the temporal variability of the local winds on bay dynamics was examined by creating a local wind forcing index and comparing composite day averaged quantities during weak and strong forcing periods. The index is defined using the normalized scale-averaged wavelet power of the local diurnal winds, as in Figure 6d. Using a nondimensional cutoff of 0.3 (results largely consistent with other thresholds, e.g., 0.2 or 0.4), Figure 10a highlights periods of strong and weak local wind forcing, respectively, consistent with the general trends in Figure 2a. The composite average of surface currents from HF radar calculated over the entire weak and strong wind periods is shown in panel (i) of Figures 10b and 10c, respectively. Large-scale flows for both periods are directed toward the south and out of the larger embayment, but the average currents are nearly double during the strong local wind forcing period. The local wind forcing index accurately delineates the two wind forcing periods, evident in the canonical day winds in Figure 10, panel (ii), where the strong wind period shows peak eastward winds that are nearly double that of the weak wind period.

Comparison of the temperature structure displays many of the same diurnal (i.e., canonical day) features described previously; however, the strong wind period shows a much sharper warm front in the early morning, and enhanced upwelling in the late evening. The enhanced upwelling is evident in the steeper isotherms and increased flux of cold, subthermocline waters to the nearshore. This leads to the cold water mass extending farther up into the water column for longer periods of time relative to the weak wind period. The velocity structure
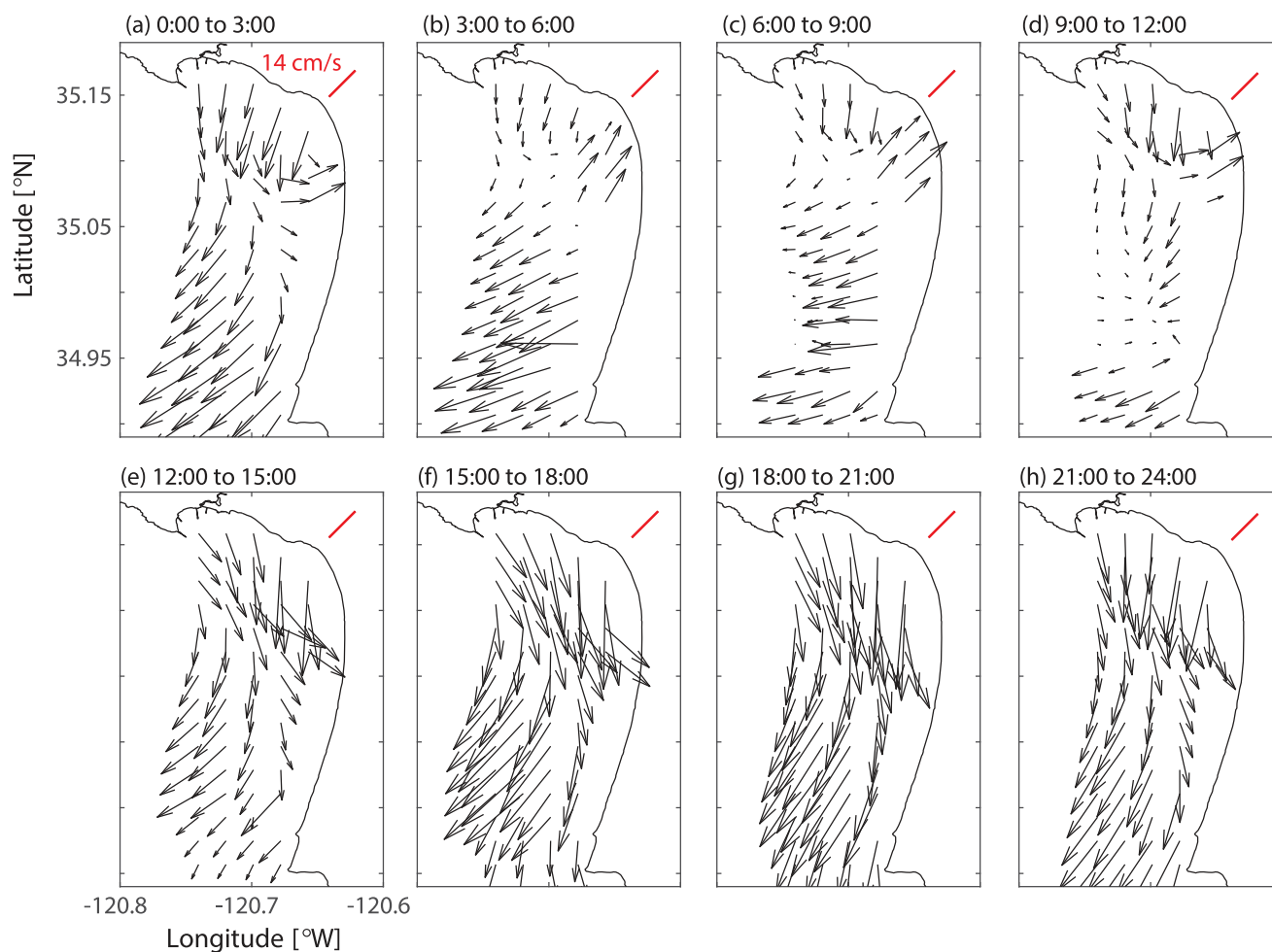
Figure 9. Composite day average plots of surface current vectors (black arrows) obtained from HF radar measurements over the entire study period. Individual panels denote composite averages taken over the time period shown at the top of each respective panel (all times in local time, PDT).

shows the same general trends, but the velocities and features (e.g., near-surface jet, shear) are intensified, particularly during the peak wind forcing around 15:00 in the strong wind period. The CEOF amplitude time series (Figure 10, panel (iii)) also shows a much more pronounced maximum coinciding with the peak in wind forcing during the strong wind period. This is in contrast to the weak wind period, which displays less diurnal structure and only a minimal afternoon increase around 15:00. The diurnal evolution of the CEOF phase is similar between the two periods, but the strong wind period shows much less variability compared to the weak wind period.

The cross-shelf evolution of temperature structure during the weak and strong wind periods is shown in Figures 11a and 11b, respectively. During the strong wind forcing period, progressively colder waters upwell to the Middle Bay and Nearshore mooring locations compared to the weak wind forcing period. Furthermore, these colder waters penetrate higher up in the water column and persist along the bottom of the water column for greater portions of the day during strong wind forcing periods. Changes in the timing and structure of the front separating the cold and warm water masses are also observed between the two periods. It is clear that the distribution of temperature, and potentially other water mass properties, in the shallow reaches of the bay is modulated by local wind forcing and this upwelling mechanism.

4. Discussion

4.1. Diurnal Heat Budget

The previous sections established a strong relationship between diurnal changes to the water column temperature structure and local wind forcing. Here we examine the effect of surface heat fluxes on the
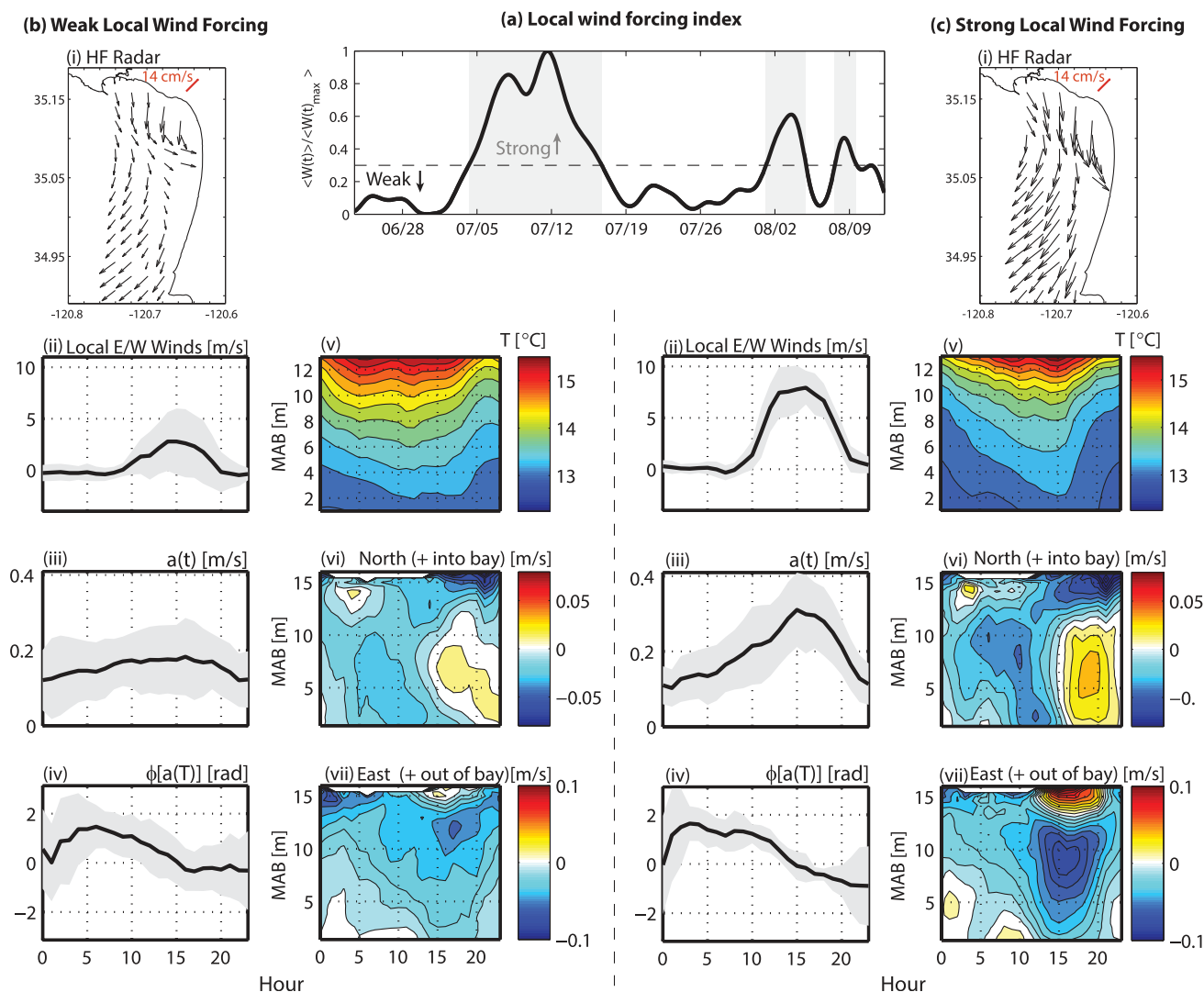
Figure 10. (a) Normalized, diurnal scale-averaged wavelet power of the local east/west winds (as in Figure 6d) used for the local diurnal wind forcing index. The dashed black line denotes the cutoff (0.3) between strong and weak wind forcing. Time periods above this cutoff (strong local wind forcing) are shaded gray. Figures 10b and 10c show the composite day averages of various parameters (subpanels (i)–(vii) described below) calculated at the Middle Bay mooring over the (b) weak and (c) strong local wind forcing periods, respectively. (i) Composite average surface current vectors from HF radar measurements over the entire strong/weak period, composite day averages of the (ii) local east/west winds, first-mode CEOF (iii) amplitude time series magnitude and (iv) phase, (v) temperature, (vi) north/south velocity (north = positive/into the bay study site), and (vii) east/west velocity (east = positive/out of the bay study site). The gray shading in subpanels (ii–iv) signifies one standard deviation from mean.

diurnal evolution of the local water column heat content. The total surface heat flux is estimated from the sum of the incoming shortwave solar radiation (Q_{sw}), latent (Q_{lat}), sensible (Q_{sens}), and outgoing longwave radiation (Q_{lw}) heat fluxes, where positive (negative) values represent heat fluxes into (out of) the ocean. Individual heat flux terms are estimated using local data from the Cal Poly Pier meteorological station and the bulk formula found in *Rosenfeld et al.* [1994] (see also *Suanda et al.* [2011]). The relative humidity sensor at the Cal Poly Pier malfunctioned during the experiment, so this parameter was obtained from a meteorological station in the nearby Morro Bay (Figure 1a, data available at www.slosea.org/about/archive.php).

Composite day averages were calculated for the individual surface heat flux terms in Figure 12a. The surface heat fluxes are dominated by the incoming shortwave solar radiation, which peaks midday, with magnitudes and relative values consistent to those in *Suanda et al.* [2011] from the nearby Monterey Bay region. The diurnal cycle of the total surface heat flux (Figure 12b) is compared to observed changes in the depth-integrated (i.e., water column) heat content,
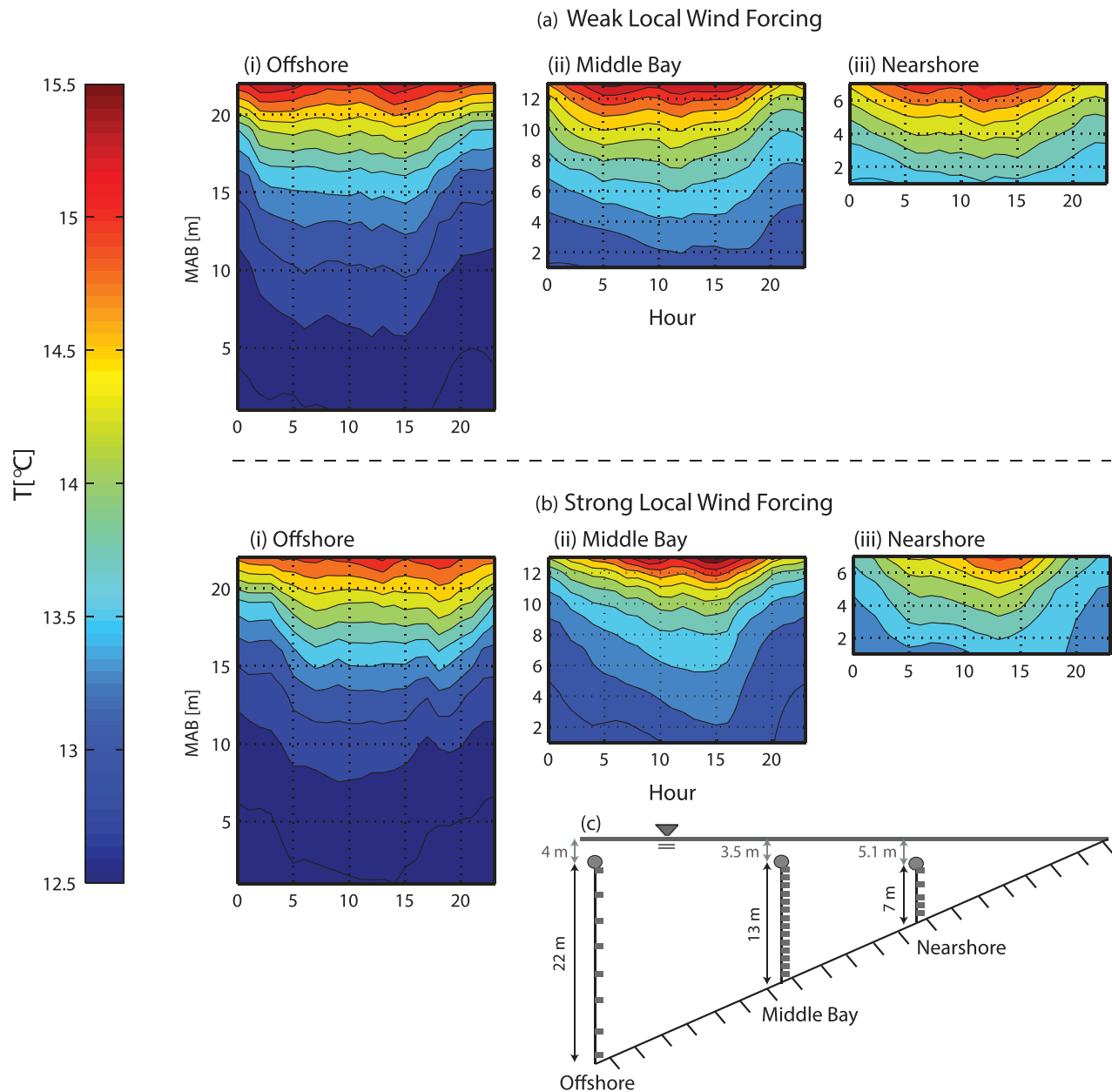
Figure 11. Composite day average plots highlighting the cross-shelf distribution of temperature calculated over the (a) weak and (b) strong local wind forcing periods, respectively. Subpanels (i), (ii), and (iii) show the composite day average temperature at the Offshore, Middle Bay, and Nearshore mooring, respectively, for the (a) weak and (b) strong diurnal wind periods. (c) Schematic of the cross-shelf array of moorings and instrumentation, where the gray rectangles denote approximate thermistor locations, the gray circle indicates the subsurface buoy location, and the black and gray lengths designate the vertical distance from the seafloor to the near-surface thermistor, and the approximate vertical distance from the near-surface thermistor to the average sea surface height over the experiment, respectively.

$$\rho c_p \int_{-H}^{0} \frac{\partial T}{\partial t}\, dz, \tag{2}$$

where ρ is the seawater density, c_p is the specific heat (3993 J/kgC), H is the water column depth, and $\frac{\partial T}{\partial t}$ is the time-derivative of the canonical day temperature. Full water column profiles of temperature were possible (see Middle Bay schematic in Figure 1d) with the incorporation of very near-surface temperature measurements obtained from an automated profiler at the end of the Cal Poly Pier (see www.cencoos.org/data/shore/sanluis for data description and access).

In general, changes to the water column heat content are due to a combination of advective and surface heat fluxes. Figure 12b highlights the daily cycle of heat content changes compared to the total surface
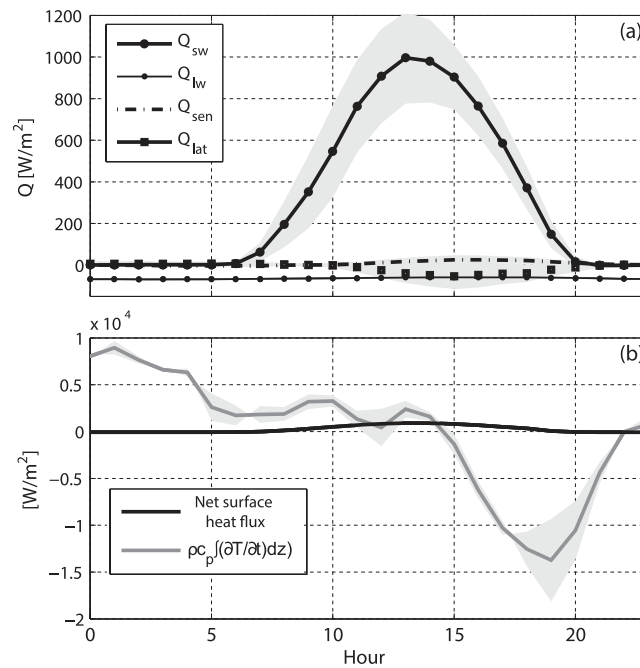
Figure 12. (a) Composite day averages of individual surface heat flux terms: incoming shortwave radiation (Q_{sw}), longwave radiation (Q_{lw}), sensible (Q_{sen}), and latent (Q_{lat}). Positive values represent heat fluxes into the ocean. (b) Composite day averages of the net surface heat flux (black line) and the change in heat content within the water column (gray line). The gray shading in both panels signifies one standard deviation from mean.

heat flux. During the early morning, there are large increases in the heat content (i.e., warming) followed by large decreases (i.e., cooling) in the late evening following the peak in the local winds. These changes to the heat content are nearly an order of magnitude larger than the maximum in the net surface heat flux, which occurs around midday. These results indicate that surface heat fluxes do not explain the large water column warming and cooling events. Rather, the changes are due to advective heat fluxes. These fluxes are likely the result of the advection of the warm water mass into the bay study site in the early morning when the winds are weak (warming) and the local upwelling of cold water into the bay study site following the peak in local winds (cooling). *Suanda et al.* [2011] found a similar minimal contribution from the surface heat flux in northern Monterey Bay. These results also suggest that the local heat budget is controlled by advective heat fluxes, which are driven by local wind forcing.

4.2. Implications

The local circulation and temperature structure within the northernmost portion of SLO Bay is predominantly controlled by local wind forcing. The diurnal forcing results in the development of a local front between the warm water mass inside the bay and cold upwelled water. The modulation of the front by local winds results in diurnal changes to the water column stratification. However, the strong near-surface shear that develops in the presence of the local winds has the ability to erode this stratification and generate local wind-driven mixing of the water column. The water column stability is assessed by comparing the stratification and velocity shear using the gradient Richardson number,

$$Ri = \frac{N^2}{\left(\frac{\partial U}{\partial z}\right)^2 + \left(\frac{\partial V}{\partial z}\right)^2}, \tag{3}$$
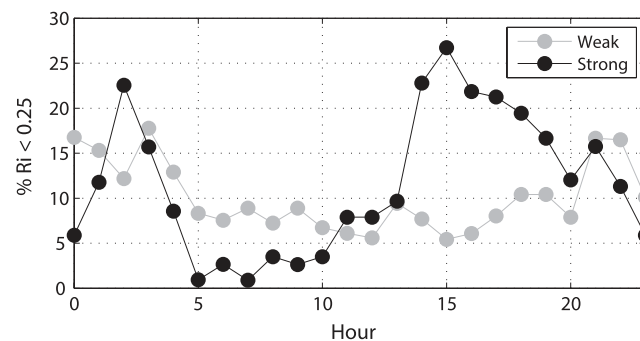

Figure 13. Percentage of time that the near-surface (13 mab) gradient Richardson number is below the critical value of 0.25 at each respective canonical day hour for the weak (gray) and strong (black) local wind forcing periods.

where $N^2 = -\frac{g}{\rho_o}\frac{\partial \rho}{\partial z}$ is the buoyancy frequency squared, and U and V denote the east and north velocity components (10 min averages), respectively. Figure 13 shows composite day averages for the strong and weak wind forcing periods, respectively, of the percentage of the time that the near-surface (13 mab) gradient Richardson number is below the critical value of 0.25. In the late afternoon (15:00, coinciding with the peak in local winds), the strong wind forcing period shows a much greater percentage of the time where the flow is subcritical

(Ri < 0.25) and is subject to the destabilizing effect of the local wind-driven shear and enhanced vertical mixing.

The combination of the local coastline orientation, topographic features, and wind forcing lead to frontogenesis and the modulation of the warm water mass inside of the bay, resulting in episodic changes to the water column stratification. Evident throughout the entire record are HFIWs that propagate along the internal wave guide (i.e., stratification) provided by the buoyant plume front (e.g., Figure 3b around 12:00 on 6 July at the base of the near-surface warm layer). Frequent occurrences of nonlinear internal waves with amplitudes exceeding half the depth of the water column are observed, as well as rank-ordered packets of HFIWs. *Woodson et al.* [2011] noted an increased prevalence of HFIWs at a coastal upwelling front during strong diurnal wind forcing, and *Woodson et al.* [2011] and *Walter et al.* [2016] hypothesized that the local winds were responsible for the transcritical generation [see *Stastna and Walter*, 2014] of internal waves at the front. Furthermore, the near-surface temperature spectra falloff rate follows a −3 power law and sharper falloff, implying a scattering of HFIWs toward smaller scales [*Nam and Send*, 2011]. A further understanding of the role that local wind forcing plays in nonlinear internal wave generation [cf. *Lerczak et al.*, 2001], as well as the subsequent fate of these waves in the nearshore and possible formation of internal bores [*Walter et al.*, 2012], will yield significant insight into turbulent mixing processes [*Davis and Monismith*, 2011; *Walter et al.*, 2014a], larval transport [*Shanks*, 1983; *Pineda*, 1994], and cross-shelf exchange of various scalars [*Boehm et al.*, 2002; *Walter et al.*, 2014b].

Additionally, the CCLME is listed as a hotspot for ecological risk due to upwelling-driven hypoxia, and it is also particularly vulnerable to ocean acidification (OA) because of this strong upwelling, representing a system with multiple stressors [*Hofmann et al.*, 2011; *Boehm et al.*, 2015]. A better understanding of the physical processes that control the transport of subthermocline waters, which are low in dissolved oxygen (DO) and pH, to the nearshore coastal environment will help address significant knowledge gaps in hypoxia/OA research. In many locations, regional-scale upwelling, which varies seasonally, sets the offshore stratification and moves the thermocline to shallower regions [e.g., *Pennington and Chavez*, 2000; *Walter and Phelan*, 2016]. However, the cross-shelf extent of this upwelling is often limited, suggesting alternative mechanisms for the final push of subthermocline waters to shallower regions. This study suggests that local wind-driven upwelling may be an important control on the delivery of subthermocline waters to shallow, nearshore habitats and needs to be considered when assessing drivers of nearshore hypoxia and OA.

From a biological perspective, local wind variability in coastal embayments likely has a considerable effect on local phytoplankton dynamics and community structure, as well as the occurrence of harmful algal blooms (HABs). Previous studies have shown that strong thermal stratification and low wind stress conditions promote retention of surface waters and favor algal blooms [*Ryan et al.*, 2008]. The results presented here indicate that weak local wind forcing reduces exchange in the bay and decreases wind-driven mixing. These conditions act to increase local residence times and allow stratified conditions to persist, which has the potential to minimize dispersal of surface aggregations and create a local bloom incubator [*Ryan et al.*, 2008]. Moreover, coastal convergent fronts have the ability to create small-scale structure and locally aggregate phytoplankton, thereby influencing plankton ecology [*Ryan et al.*, 2010]. Finally, it is interesting to consider the role that SLO Bay plays in the broader ecology of the region, as Point Conception (80 km to the south) is a major biogeographic province boundary. At the regional scale, Point Conception demarcates the northern open coast dominated by cold upwelled waters from the warmer, sheltered waters of the Southern California Bight to the south [*Caldwell et al.*, 1986; *Blanchette et al.*, 2007; *Aristizabal et al.*, 2016]. Preliminary analysis of data from long-term temperature records in the area (Walter et al., unpublished manuscript) indicates that SLO Bay behaves as an upwelling shadow system. This, combined with the periodic warming of SLO Bay generated by the diurnal wind relaxation, may promote favorable conditions for a refuge for organisms expanding northward, although further work is needed to verify this hypothesis.

In general, regional and local-scale processes interact to drive substantial physical and biological variability in the coastal ocean. While the current generation of coastal circulation models is able to accurately capture larger-scale flows, modeling processes on smaller scales continues to pose challenges [*Rasmussen et al.*, 2009]. In particular, coastline topography and high-resolution wind forcing data have been shown to be important parameters to accurately capture nearshore physics and larval dispersal patterns [see *Rasmussen et al.*, 2009, and the references therein]. This study reinforces the idea that careful consideration of the grid

resolution and wind forcing, especially in small coastal embayments, is needed to adequately resolve important nearshore physics and biological processes such as larval dispersal.

5. Conclusions

Coastal embayments are ubiquitous features in major upwelling systems around the world, ranging in size, shape, and dominant physical forcing. Compared to regional-scale upwelling/relaxation events, less is known about the oceanic response in these shallow systems to high-frequency local diurnal wind forcing. Understanding how these different systems are influenced by both regional and local dynamics is critical to understanding a host of physical and biological processes. In this study, we show that the local diurnal wind forcing is the dominant driver of temperature variance and circulation patterns in a small-scale coastal embayment along an understudied stretch of the central California coast. The interaction between the local wind forcing and existing stratification leads to a dynamic situation characterized by the delivery of subthermocline waters to shallow reaches of the bay. Future studies should examine the influence of local wind forcing on this upwelling mechanism across an annual cycle. It is expected that local wind forcing will play an important role in nearshore dynamics and local upwelling from the early spring to late fall when regional-scale upwelling brings the offshore thermocline closer to the surface and strong gradients between air temperatures over the land and ocean result in enhanced local wind forcing. Moreover, small-scale spatial structure in thermal structure and variability should be considered at other bay locations to better understand drivers of spatial similarities and differences, as well as outside of the bay to investigate spatial differences in regions that are subject to differential exposure to regional upwelling processes.

References

Aristizabal, M. F., M. R. Fewings, and L. Washburn (2016), Contrasting spatial patterns in the diurnal and semidiurnal temperature variability in the Santa Barbara Channel, California, *J. Geophys. Res. Oceans*, *121*, 427–440, doi:10.1002/2015JC011239.

Blanchette, C. A., B. Helmuth, and S. D. Gaines (2007), Spatial patterns of growth in the mussel, Mytilus californianus, across a major oceanographic and biogeographic boundary at Point Conception, California, USA, *J. Exp. Mar. Biol. Ecol.*, *340*(2), 126–148, doi:10.1016/j.jembe.2006.09.022.

Boehm, A. B., B. F. Sanders, and C. D. Winant (2002), Cross-shelf transport at Huntington Beach. Implications for the fate of sewage discharged through an offshore ocean outfall, *Environ. Sci. Technol.*, *36*(9), 1899–1906, doi:10.1021/es0111986.

Boehm, A. B., M. Z. Jacobson, M. J. O'Donnell, M. Sutula, W. W. Wakefield, S. B. Weisberg, and E. Whiteman (2015), Ocean acidification science needs for natural resource managers of the North American west coast, *Oceanography*, *28*(2), 170–181, doi:10.5670/oceanog.2015.40.

Bonicelli, J., C. Moffat, S. A. Navarrete, J. L. Largier, and F. J. Tapia (2014a), Spatial differences in thermal structure and variability within a small bay: Interplay of diurnal winds and tides, *Cont. Shelf Res.*, *88*, 72–80, doi:10.1016/j.csr.2014.07.009.

Bonicelli, J., F. J. Tapia, and S. A. Navarrete (2014b), Wind-driven diurnal temperature variability across a small bay and the spatial pattern of intertidal barnacle settlement, *J. Exp. Mar. Biol. Ecol.*, *461*, 350–356, doi:10.1016/j.jembe.2014.09.003.

Breaker, L. C., and W. W. Broenkow (1994), The circulation of Monterey Bay and related processes, *Oceanogr. Mar. Biol. Annu. Rev.*, *32*, 1–64.

Caldwell, P. C., D. W. Stuart, and K. H. Brink (1986), Mesoscale wind variability near Point Conception, California during spring 1983, *J. Clim. Appl. Meteorol.*, *25*, 1241–1254.

Cheriton, O. M., E. E. McPhee-Shaw, C. D. Storlazzi, K. J. Rosenberger, W. J. Shaw, and B. Y. Raanan (2014), Upwelling rebound, ephemeral secondary pycnoclines, and the creation of a near-bottom wave guide over the Monterey Bay continental shelf, *Geophys. Res. Lett.*, *41*, 8503–8511, doi:10.1002/2014GL061897.

Davis, K. A., and S. G. Monismith (2011), The modification of bottom boundary layer turbulence and mixing by internal waves shoaling on a barrier reef, *J. Phys. Oceanogr.*, *41*(11), 2223–2241, doi:10.1175/2011JPO4344.1.

Edwards, C. R., and H. E. Seim (2008), Complex EOF analysis as a method to separate barotropic and baroclinic velocity structure in shallow water, *J. Atmos. Oceanic Technol.*, *25*(5), 808–821, doi:10.1175/2007JTECHO562.1.

Emery, W. J., and R. E. Thomson (2004), *Data Analysis Methods in Physical Oceanography*, 2nd ed., 638 pp., Elsevier, Amsterdam.

García-Reyes, M., and J. L. Largier (2012), Seasonality of coastal upwelling off central and northern California: New insights, including temporal and spatial variability, *J. Geophys. Res.*, *117*, C03028, doi:10.1029/2011JC007629.

Gille, S. T., S. G. Llewellyn Smith, and S. M. Lee (2003), Measuring the sea breeze from QuikSCAT Scatterometry, *Geophys. Res. Lett.*, *30*(3), 1114, doi:10.1029/2002GL016230.

Gille, S. T., S. G. Llewellyn Smith, and N. M. Statom (2005), Global observations of the land breeze, *Geophys. Res. Lett.*, *32*, L05605, doi:10.1029/2004GL022139.

Graham, W. M., and J. L. Largier (1997), Upwelling shadows as nearshore retention sites: The example of northern Monterey Bay, *Cont. Shelf Res.*, *17*, 509–532, doi:10.1016/S0278-4343(96)00045-3.

Hickey, B. M. (1979), The California current system—Hypotheses and facts, *Prog. Oceanogr.*, *8*(4), 191–279, doi:10.1016/0079-6611(79)900002-8.

Hofmann, A. F., E. T. Peltzer, P. M. Walz, and P. G. Brewer (2011), Hypoxia by degrees: Establishing definitions for a changing ocean, *Deep Sea Res., Part I*, *58*(12), 1212–1226, doi:10.1016/j.dsr.2011.09.004.

Kaihatu, J. M., R. A. Handler, G. O. Marmorino, and L. K. Shay (1998), Empirical orthogonal function analysis of ocean surface currents using complex and real-vector methods, *J. Atmos. Oceanic Technol.*, *15*(4), 927–941, doi:10.1175/1520-0426(1998)015 < 0927: EOFAOO>2.0.CO;2.

Kämpf, J. (2015a), Interference of wind-driven and pressure gradient-driven flows in shallow homogeneous water bodies, *Ocean Dyn.*, *65*(11), 1399–1410, doi:10.1007/s10236-015-0882-2.

Kämpf, J. (2015b), Undercurrent-driven upwelling in the northwestern Arafura Sea, *Geophys. Res. Lett.*, *42*, 9362–9368, doi:10.1002/2015GL066163.

Kaplan, D. M., J. L. Largier, S. Navarrete, R. Guiñez, and J. C. Castilla (2003), Large diurnal temperature fluctuations in the nearshore water column, *Estuarine Coastal Shelf Sci.*, *57*(3), 385–398, doi:10.1016/S0272-7714(02)00363-3.

Lerczak, J. A., M. C. Hendershott, and C. D. Winant (2001), Observations and modeling of coastal internal waves driven by a diurnal sea breeze, *J. Geophys. Res.*, *106*, 19,715–19,729, doi:10.1029/2001JC000811.

Lucas, A. J., G. C. Pitcher, T. A. Probyn, and R. M. Kudela (2014), The influence of diurnal winds on phytoplankton dynamics in a coastal upwelling system off southwestern Africa, *Deep Sea Res., Part II*, *101*, 50–62, doi:10.1016/j.dsr2.2013.01.016.

Nam, S., and U. Send (2011), Direct evidence of deep water intrusions onto the continental shelf via surging internal tides, *J. Geophys. Res.*, *116*, C05004, doi:10.1029/2010JC006692.

Nidzieko, N. J., and J. L. Largier (2013), Inner shelf intrusions of offshore water in an upwelling system affect coastal connectivity, *Geophys. Res. Lett.*, *40*, 5423–5428, doi:10.1002/2013GL056756.

Orlić, M., G. Beg Paklar, V. Dadić, N. Leder, H. Mihanović, M. Pasarić, and Z. Pasarić (2011), Diurnal upwelling resonantly driven by sea breezes around an Adriatic island, *J. Geophys. Res.*, *116*, C09025, doi:10.1029/2011JC006955.

Pawlowicz, R., B. Beardsley, and S. Lentz (2002), Classical tidal harmonic analysis including error estimates in MATLAB using T_TIDE, *Comput. Geosci.*, *28*(8), 929–937, doi:10.1016/S0098-3004(02)00013-4.

Pennington, J. T., and F. P. Chavez (2000), Seasonal fluctuations of temperature, salinity, nitrate, chlorophyll and primary production at station H3/M1 over 1989-1996 in Monterey Bay, California, *Deep Sea Res., Part II*, *47*(5–6), 947–973, doi:10.1016/S0967-0645(99)00132-0.

Pineda, J. (1994), Internal tidal bores in the nearshore: Warm-water fronts, seaward gravity currents and the onshore transport of neustonic larvae, *J. Mar. Res.*, *52*(3), 427–458, doi:10.1357/0022240943077046.

Rasmussen, L. L., B. D. Cornuelle, L. A. Levin, J. L. Largier, and E. Di Lorenzo (2009), Effects of small-scale features and local wind forcing on tracer dispersion and estimates of population connectivity in a regional scale circulation model, *J. Geophys. Res.*, *114*, C01012, doi:10.1029/2008JC004777.

Rosenfeld, L. K. (1988), Diurnal period wind stress and current fluctuations over the continental shelf off northern California, *J. Geophys. Res.*, *93*(C3), 2257–2276, doi:10.1029/JC093iC03p02257.

Rosenfeld, L. K., F. B. Schwing, N. Garfield, and D. E. Tracy (1994), Bifurcated flow from an upwelling center: A cold water source for Monterey Bay, *Cont. Shelf Res.*, *14*(9), 931–964.

Rosenfeld, L., I. Shulman, M. Cook, J. Paduan, and L. Shulman (2009), Methodology for a regional tidal model evaluation, with application to central California, *Deep Sea Res., Part II*, *56*(3–5), 199–218, doi:10.1016/j.dsr2.2008.08.007.

Roughgarden, J, J. T. Pennington, D. Stoner, S. Alexander, K. Miller (1991), Collisions of upwelling fronts with the intertidal zone: The cause of recruitment pulses in barnacle populations of central California, *Acta Oecol.*, *12*, 35–51.

Ryan, J. P., J. F. R. Gower, S. A. King, W. P. Bissett, A. M. Fischer, R. M. Kudela, Z. Kolber, F. Mazzillo, E. V. Rienecker, and F. P. Chavez (2008), A coastal ocean extreme bloom incubator, *Geophys. Res. Lett.*, *35*, L12602, doi:10.1029/2008GL034081.

Ryan, J. P., A. M. Fischer, R. M. Kudela, M. A. McManus, J. S. Myers, J. D. Paduan, C. M. Ruhsam, C. B. Woodson, and Y. Zhang (2010), Recurrent frontal slicks of a coastal ocean upwelling shadow, *J. Geophys. Res.*, *115*, C12070, doi:10.1029/2010JC006398.

Send, U., R. C. Beardsley, C. D. Winant (1987), Relaxation from upwelling in the coastal ocean dynamics experiment, *J. Geophys. Res.*, *92*(C2), 1683–1698, doi:10.1029/JC092iC02p01683.

Shanks, A. (1983), Surface slicks associated with tidally forced internal waves may transport pelagic larvae of benthic invertebrates and fishes shoreward, *Mar. Ecol. Prog. Ser.*, *13*, 311–315, doi:10.3354/meps013311.

Stastna, M., and R. K. Walter (2014), Transcritical generation of nonlinear internal waves in the presence of background shear flow, *Phys. Fluids*, *26*, 086601, doi:10.1063/1.4891871.

Suanda, S. H., J. A. Barth, and C. B. Woodson (2011), Diurnal heat balance for the northern Monterey Bay inner shelf, *J. Geophys. Res.*, *116*, C09030, doi:10.1029/2010JC006894.

Torrence, C., and G. P. Compo (1998), A practical guide to wavelet analysis, *Bull. Am. Meteorol. Soc.*, *79*, 61–78, doi:10.1175/1520-0477(1998)079<0061:APGTWA>2.0.CO;2.

Walter, R. K., and P. J. Phelan (2016), Internal bore seasonality and tidal pumping of subthermocline waters at the head of the Monterey submarine canyon, *Cont. Shelf Res.*, *116*, 42–53, doi:10.1016/j.csr.2016.01.015.

Walter, R. K., N. J. Nidzieko, and S. G. Monismith (2011), Similarity scaling of turbulence spectra and cospectra in a shallow tidal flow, *J. Geophys. Res.*, *116*, C10019, doi:10.1029/2011JC007144.

Walter, R. K., C. B. Woodson, R. S. Arthur, O. B. Fringer, and S. G. Monismith (2012), Nearshore internal bores and turbulent mixing in southern Monterey Bay, *J. Geophys. Res.*, *117*, C07017, doi:10.1029/2012JC008115.

Walter, R. K., M. E. Squibb, C. B. Woodson, J. R. Koseff, and S. G. Monismith (2014a), Stratified turbulence in the nearshore coastal ocean: Dynamics and evolution in the presence of internal bores, *J. Geophys. Res. Oceans*, *119*, 8709–8730, doi:10.1002/2014JC010396.

Walter, R. K., C. B. Woodson, P. R. Leary, and S. G. Monismith (2014b), Connecting wind-driven upwelling and offshore stratification to nearshore internal bores and oxygen variability, *J. Geophys. Res. Oceans*, *119*, 3517–3534, doi:10.1002/2014JC009998.

Walter, R. K., M. Stastna, C. B. Woodson, and S. G. Monismith (2016), Observations of nonlinear internal waves at a persistent coastal upwelling front, *Cont. Shelf Res.*, *117*, 100–117, doi:10.1016/j.csr.2016.02.007.

Washburn, L., M. R. Fewings, C. Melton, and C. Gotschalk (2011), The propagating response of coastal circulation due to wind relaxations along the central California coast, *J. Geophys. Res.*, *116*, C12028, doi:10.1029/2011JC007502.

Wing, S. R., L. W. Botsford, J. L. Largier, and L. E. Morgan (1995), Spatial structure of relaxation events and crab settlement in the northern California upwelling system, *Mar. Ecol. Prog. Ser.*, *128*(1–3), 199–211, doi:10.3354/meps128199.

Woodson, C. B., et al. (2007), Local diurnal upwelling driven by sea breezes in northern Monterey Bay, *Cont. Shelf Res.*, *27*(18), 2289–2302, doi:10.1016/j.csr.2007.05.014.

Woodson, C. B., L. Washburn, J. A. Barth, D. J. Hoover, A. R. Kirincich, M. A. McManus, J. P. Ryan, and J. Tyburczy (2009), Northern Monterey Bay upwelling shadow front: Observations of a coastally and surface-trapped buoyant plume, *J. Geophys. Res.*, *114*, C12013, doi:10.1029/2009JC005623.

Woodson, C. B., et al. (2011), Observations of internal wave packets propagating along-shelf in northern Monterey Bay, *Geophys. Res. Lett.*, *38*, L01605, doi:10.1029/2010GL045453.